



Contents lists available at ScienceDirect

Journal of Power Sources

journal homepage: [www.elsevier.com/locate/jpowsour](http://www.elsevier.com/locate/jpowsour)



## Three-dimensional modeling of hydrogen sorption in metal hydride hydrogen storage beds

Yun Wang<sup>a,\*</sup>, Xavier Cordobes Adroher<sup>a</sup>, Jixin Chen<sup>a</sup>, Xiao Guang Yang<sup>b</sup>, Ted Miller<sup>b</sup>

<sup>a</sup> Renewable Energy Resources Lab (RERL) and National Fuel Cell Research Center, Department of Mechanical and Aerospace Engineering, The University of California, Irvine, 4200 Engineering Gateway, Irvine, CA 92697-3975, USA

<sup>b</sup> Advanced Battery Technologies, Research and Innovation Center, Ford Motor Company, Dearborn, MI 48120, USA

### ARTICLE INFO

#### Article history:

Received 29 April 2009

Received in revised form 16 June 2009

Accepted 16 June 2009

Available online xxx

#### Keywords:

Hydrogen storage

Modeling

Numerical simulation

Three dimensions

LaNi<sub>5</sub>

### ABSTRACT

This paper conducts a three-dimensional (3D) modeling study to investigate the hydrogen absorption process and associated mass and heat transport in a metal hydride (LaNi<sub>5</sub>) hydrogen storage tank. The 3D model is further implemented numerically for validation purpose and the detailed investigation on absorption process. Results indicate that at the very initial absorption stage the bed temperature evolves almost uniformly, while it varies greatly spatially at the latter stage. At the initial seconds, most hydrogen is absorbed in the region near the cooling wall due to the better heat removal. The absorption in the core is slow at the beginning, but becomes important at the very end stage. It also shows that the initial hydrogen flow in the bed is several-fold larger than the latter stage and the flow may provide extra cooling to the hydriding process. By analyzing the Peclet number, we find that the heat convection by the hydrogen flow may play an important role in local heat transfer. This work provides an important platform beneficial to the fundamental understanding of multi-physics coupling phenomena during hydrogen absorption and the development of on-board hydrogen storage technology.

© 2009 Elsevier B.V. All rights reserved.

### 1. Introduction

Hydrogen as an alternative energy source has been receiving great attention worldwide due to the growing demand for environmentally clean fuels to replace nonrenewable carbonaceous fuels such as gasoline [1]. Hydrogen storage is one of the central technical barriers to the wide deployment of hydrogen energy, particularly for automotive applications (e.g. hydrogen fuel cell vehicles). Current hydrogen storage methods including gas compression and liquefaction are not optimal for onboard applications due to the associated large quantity of energy consumption and safety issues. A promising alternative is solid-metal hydride storage: utilizing metal hydrides to absorb/desorb hydrogen at relatively low pressures (<20 bar), which offers safety and cost advantage, however, the obvious disadvantage of weight for hydrogen onboard storage.

Developing effective solid-state hydrogen storage for transportation is crucial for the success of the hydrogen economy. Besides energy density and system cost requirements, one important requirement by transportation applications is fast kinetics of hydrogen storage, i.e. quick charge and discharge. For instance, refu-

eling time for automobiles must be short in minutes in order to compete with traditional combustors. In addition, dynamic characteristics of hydrogen release should satisfy the need of the fast load variation. To develop such effective storage systems, physics of the transport process coupled with reaction kinetics are highly in need, such as hydrogen mass flow in the hydride bed, heat transfer within the bed, and local hydrogen absorption rate.

Fundamental modeling of hydrogen storage has been attempted by several groups. Jemni and Nasrallah [2] developed a two-dimensional model for the hydrogen storage LaNi<sub>5</sub>-H<sub>2</sub> system. Efforts were also made to experimentally determine the reaction kinetics, equilibrium pressure, and thermal conductivity [3]. Nakagawa et al. [4] present a two-dimensional model for heat and mass transfer within the LaNi<sub>5</sub> alloy bed. They found that the absorption rate may be limited by heat transfer due to the low thermal conductivity of the alloy bed, therefore external cooling/heating may play an important role in the hydriding/dehydriding process. Mat and Kaplan [5] developed a two-dimensional model consisting of heat and mass transfer and chemical reaction in the LaNi<sub>5</sub> storage tank bed. They found that the hydride formation enhances at lower equilibrium pressure regions and the hydrogen absorption rate slows down due to the reaction heat that increases the bed temperature. Other modeling approaches include Refs. [6–9], which investigate the hydriding/dehydriding process and examine the factors that affect the tank performance.

\* Corresponding author. Tel.: +1 949 824 6004; fax: +1 949 824 8585.  
E-mail address: [yunw@uci.edu](mailto:yunw@uci.edu) (Y. Wang).

### Nomenclature

Bi	the Biot number
$c_p$	specific heat, $\text{J kg}^{-1} \text{K}^{-1}$
$D$	diameter of molecule (m)
$E_a$	activation energy
H/M	hydrogen to metal atomic ratio
$\Delta H^0$	reaction heat of formation ( $\text{J kg}^{-1}$ )
$h$	heat transfer coefficient ( $\text{W m}^{-2} \text{K}^{-1}$ )
$k$	thermal conductivity ( $\text{W m}^{-1} \text{K}^{-1}$ )
$M$	molecular weight ( $\text{kg mol}^{-1}$ )
$n$	the direction normal to the surface
$P$	pressure (bar)
Pr	Prandtl number
$r$	radius (m)
$R$	universal gas constant, $8.134 \text{ J mol}^{-1} \text{K}^{-1}$
Re	Reynolds number
$S$	source term
$t$	time (s)
$T$	temperature (K)
$\vec{u}$	velocity vector ( $\text{m s}^{-1}$ )

### Greek letters

$\alpha$	thermal diffusivity ( $\text{m}^2 \text{s}^{-1}$ )
$\rho$	density ( $\text{kg m}^{-3}$ )
$\varepsilon$	porosity

### Superscripts and subscripts

<i>eq</i>	equilibrium
<i>eff</i>	effective value
<i>g</i>	gas phase
<i>m</i>	mass
<i>s</i>	solid; saturation

Though great efforts have been made in the hydrogen storage of metal hydride beds, study of detailed distribution and evolution is highly in need to investigate the local hydriding process, coupled transport and associated limiting factors as well as the characteristics of different hydriding stages. This paper seeks to develop a 3D model of the hydriding process coupled with mass/heat transport in the hydrogen tank and explore these issues that are extremely important for efficient hydrogen storage. The model is validated with published experimental data and further applied to investigate mass/heat transport and reaction kinetics during the hydriding process.

## 2. Mathematical modeling

During the hydriding process, hydrogen is injected to a storage tank and transported via the interstitial space of the packed alloy particles, reacting with the unconsolidated metal particles. In addition to mass transport, the hydriding process is exothermic and temperature has profound impacts on reaction kinetics, therefore heat production and transfer within the tank must be included to investigate the hydrogen adsorption. To develop a mathematical model that describes the hydriding process, the following assumptions are made: (1) the flow bed can be treated as a homogeneous porous media with uniform morphological properties, such as porosity, tortuosity and permeability; (2) the ideal gas law holds true in the gas phase; (3) local solid and fluid are in thermal equilibrium.

### 2.1. Mass transport

Gaseous hydrogen flows through the bed and reacts with the hydride metal. The mass conservation of hydrogen can be written as

$$\frac{\partial \varepsilon \rho^g}{\partial t} + \nabla \cdot \rho^g \vec{u} = -S_m \quad (1)$$

where  $S_m$  is the local hydrogen absorption reaction rate and  $\vec{u}$  the superficial velocity. The metal hydride tank is typically characterized as a porous medium packed with alloy particles. The Darcy's law can be applied to describe the hydrogen flow:

$$\rho^g \vec{u} = -\frac{K}{\nu^g} (\nabla P - \rho^g \vec{g}) \quad (2)$$

where the permeability  $K$  is calculated through the Blake–Kozeny equation that relates  $K$  to the alloy particle radius and bed porosity [10]:

$$K = \frac{D_p^2}{150} \frac{\varepsilon^3}{(1 - \varepsilon)^2} \quad (3)$$

where  $D_p$  is the particle diameter and  $\varepsilon$  the porosity. For a typical size of particles ( $D_p \sim 1 \text{ mm}$ ) and  $\varepsilon \sim 0.5$ ,  $K$  is  $10^{-8}$  to  $10^{-9} \text{ m}^2 \text{ s}^{-1}$ .

In the expansion region where there are no solid particles, the Navier–Stokes equation applies. A single-domain description can be formulated with a general moment equation:

$$\frac{1}{\varepsilon} \left[ \frac{\partial \rho^g \vec{u}}{\partial t} + \frac{1}{\varepsilon} \nabla \cdot (\rho^g \vec{u} \vec{u}) \right] = -\nabla P + \nabla \cdot \tau + S_u + \rho^g \vec{g} \quad (4)$$

where  $\vec{u}$  is the superficial velocity. The source term  $S_u$  describes the Darcy's forces  $(-\mu/K)\vec{u}$ , which is zero in the expansion region. Note that Eq. (1) gives a general expression for the mass conservation that can be applied in both porous bed and expansion region, e.g. for the expansion region, the porosity is 1 and the source term  $S_m$  becomes zero. The gas density is calculated through the ideal gas law:

$$\rho^g = \frac{PM_{H_2}}{RT} \quad (5)$$

### 2.2. Heat transport

The energy equation in the porous bed can be expressed as

$$\frac{\partial \bar{\rho} \bar{c}_p T}{\partial t} + \nabla \cdot (\rho^g \bar{c}_p \vec{u} T) = \nabla \cdot (k^{eff} \nabla T) + S_T \quad (6)$$

where

$$\bar{\rho} \bar{c}_p = (1 - \varepsilon) \rho^s c_p^s + \varepsilon \rho^g c_p^g, \quad k^{eff} = (1 - \varepsilon)^{\tau_s} k^s + \varepsilon^{\tau_g} k^g, \quad \text{and}$$

$$S_T = S_m [\Delta H^0 - (c_p^g - c_p^s)] \quad (7)$$

Note that the thermal conductivity of the solid is much higher than hydrogen, therefore the contribution from hydrogen can be neglected. In addition, the interfacial contact resistance among the metal particles may contribute to a considerable portion of the thermal resistance, which is included in the tortuosity of the solid matrix  $\tau_s$ . In the literature, the value of  $k^{eff}$  is around  $1 \text{ W m}^{-1} \text{K}^{-1}$ .

### 2.3. Hydriding reaction kinetics

The following reaction takes place at the absorption sites of the alloy (LaNi<sub>5</sub>):



As the alloy particles are solid, the gaseous hydrogen first enters the particle via the surface. The H atom within the metal alloy

may vibrate around alloy atom forming H–M bond or take multiple hops among metal alloy atoms which may be the major mechanism for hydrogen transport within the alloy [11,12]. As stated by Zhang and Angell [13], the stochastic nature of such long-range multi-step jumps can be modeled as the Fick’s diffusion. Such a process within a metal particle is usually simplified as shrinking core or contracting-envelop model where the reaction occurs at the moving interface between unreacted core (also called  $\alpha$ -phase) and reacted shell (also called  $\beta$ -phase) [13,14]. In the present macroscopic model, we deal with representative volumes which contain a sufficiently large number of metal particles in each volume. The local reaction rate is the average over these particles in the representative volume. In addition, the volume fraction of the solid is uniform among the representative volumes and hence equal to  $1 - \varepsilon$ . The equation of the reacted mass, the  $\beta$ -phase, can then be expressed as

$$(1 - \varepsilon) \frac{\partial \rho^s}{\partial t} = S_m \quad (9)$$

The hydrogen reaction rate is a function of temperature, equilibrium pressure, and the portion of unreacted alloy

$$S_m = -C_a \exp\left(-\frac{E_a}{RT}\right) \ln\left(\frac{P_g}{P_{eq}}\right) (\rho_s^s - \rho^s) \quad (10)$$

where  $C_a$  is a constant for specific material of hydride metals. For LaNi<sub>5</sub>, its value is 59.187 s<sup>-1</sup> [9,15].  $\rho_s^s$  represents the saturated metal density. The equilibrium pressure  $P_{eq}$  can be calculated through the Van’t Hoff relationship. Jemni and Nasrallah [16] and Aldas et al. [17] adopted the following form that directly shows the dependence of the equilibrium pressure on the absolute temperature:

$$\ln P_{eq} = A - \frac{B}{T} \quad \text{with } A = 52.5 \text{ and } B = 43876.45 \text{ K} \quad (11)$$

Jemini et al. [3] further experimentally measured the  $P$ – $C$ – $T$  (pressure–concentration–temperature) curves at different temperatures. Starting with the Van’t Hoff equation

$$\ln P_{eq} = \frac{\Delta H}{RT} - \frac{\Delta S}{R} \quad (12)$$

where the entropy change  $\Delta S$  relates to the value of H/M (the hydrogen-to-metal ratio), they determined the equilibrium pressure as a polynomial function of H/M, which is shown in Fig. 1. Fig. 1 indicates that at low H/Ms  $P_{eq}$  decreases rapidly with H/M.

#### 2.4. Boundary and initial conditions

Eqs. (1), (4), (6) and (9) forms a complete set of governing equations with six unknowns:  $\vec{u}$  (three components),  $P$ ,  $T$ , and  $\rho^s$ . Their corresponding initial and boundary conditions are described as follow:

Initial conditions:

$$\begin{pmatrix} \vec{u} \\ P \\ T \\ \rho^s \end{pmatrix} = \begin{pmatrix} 0 \\ P_0 \\ T_0 \\ \rho_0^s \end{pmatrix} \quad (13)$$

**Inlet Boundaries:** The inlet conditions are set according to the specified temperature, flow rate and pressure.

**Walls:** No-slip and impermeable velocity condition and no-flux condition are applied, while for the thermal equation a convection boundary condition is adopted:

$$-k^{eff} \frac{\partial T}{\partial n} \Big|_{wall} = h(T - T_\infty) \quad (14)$$

where  $n$  is the direction normal to the tank outer surface or the interface between the tank and cooling flow. Note that from this

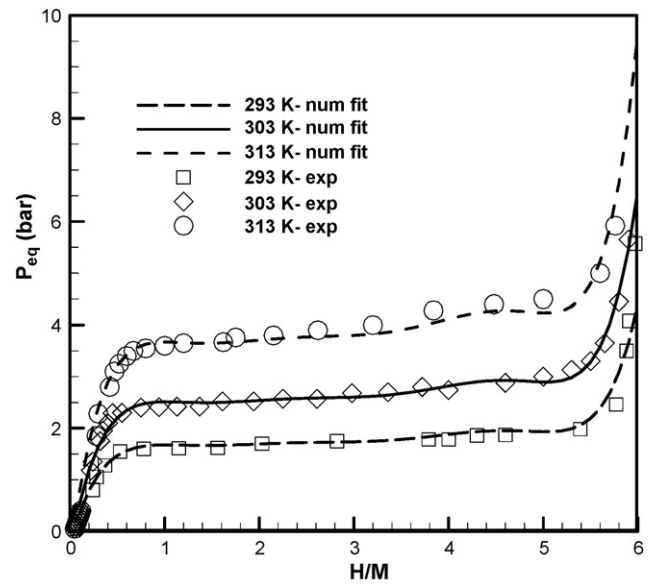


Fig. 1.  $P_{eq}$  as a function of the H/M ratio and temperature. The numerical fit adopts the 7th order polynomial suggested by Ref. [19], i.e.  $a_0 = -0.34863$ ,  $a_1 = 10.1059$ ,  $a_2 = -14.2442$ ,  $a_3 = 10.3535$ ,  $a_4 = -4.20646$ ,  $a_5 = 0.962371$ ,  $a_6 = -0.115468$ ,  $a_7 = 0.00563776$  (reproduced from Ref. [19]).

boundary condition, one can obtain a dimensionless parameter Bi (Biot) number to compare the convection at the tank surface and conduction within the porous bed

$$Bi = \frac{hL_c}{k^{eff}} \quad (15)$$

where  $L_c$  is the characteristic length of the tank. The heat transfer coefficient  $h$  is primarily determined by the cooling fluid. For air natural convection cooling,  $h$  is around 1–10 W(m<sup>2</sup>K)<sup>-1</sup> while the forced convection may increase its value to 30–100 W(m<sup>2</sup>K)<sup>-1</sup>. For a small-scale tank, e.g.  $L_c < 5$  mm, where  $Bi < 1$ , temperature is almost uniform within the tank. For larger units or advanced cooling systems with high  $h$ s, where the Bi value is well above 1, temperature varies spatially within the hydride bed. For the hydrogen storage tank considered in this paper,  $Bi \gg 1$ .

### 3. Numerical procedures

The governing equations along with their appropriate boundary conditions are discretized by the finite volume method, with SIMPLE (semi-implicit pressure linked equation) algorithm [18]. For the finite-volume discretization, it is convenient to unify all governing equations, including the transient terms, in the following form:

$$\frac{\partial \Theta}{\partial t} + \nabla \cdot \vec{\Gamma}(\Theta) = S_\Theta \quad (16)$$

where  $\Theta$  stands for any dependent variable in the governing equations. Integrating the above equation throughout an arbitrary volume  $V$  bounded by a closed surface  $S$ , yields:

$$\int_V \frac{\partial \Theta}{\partial t} dv + \oint_S \vec{\Gamma}(\Theta) \cdot d\vec{S} = \int_V S_\Theta dv \quad (17)$$

where  $\vec{S}$  is the surface vector. Taking  $V$  and  $S$  to be the volume  $V_p$  and discrete faces,  $S_j$ , of a computational cell, respectively, which is fixed, one can reach:

$$\frac{\partial}{\partial t} \int_{V_p} \Theta dv + \sum_j \int_{S_j} \vec{\Gamma}(\Theta) \cdot d\vec{S} = \int_{V_p} S_\Theta dv \quad (18)$$

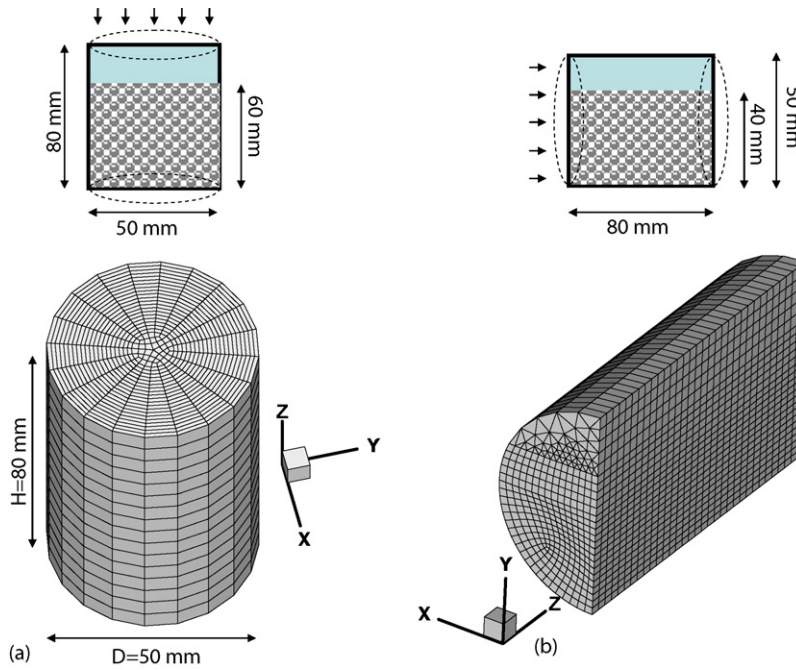


Fig. 2. Geometry and computational domain of the hydrogen tank: (a) Scenario #1; (b) Scenario #2.

The final form of the discrete finite volume equation can be expressed as

$$B_p \Theta_p^n = \sum_m B_m \Theta_m^n + B(\Theta_p^0) \quad (19)$$

The above equation is then solved by the algebraic multi-grid (AMG) method.

The geometry and computational meshes of a cylindrical hydrogen tank for a numerical study are shown in Fig. 2. Only the region of  $z < 60$  mm (for Scenario #1) is filled with the hydride particles. The part of  $z > 60$  mm is the expansion region of the bed. Due to the geometrical symmetry, Scenario #1 can be treated as a two-dimensional case. To demonstrate the 3D capability of the model, we also consider another case with the same geometry but different arrangement of the tank, i.e. Scenario #2, or the tank is laid down horizontally, see Fig. 2 (b). The masses of the metal hydride in the tanks are comparable for the two scenarios. In this study, we exclude the expansion mechanism of alloy particles in the model and assume that the expansion region is hollow space without any metal particles. About 24,000 computational cells are used to capture the coupling of hydriding kinetics and heat/mass transport. Geometrical and operating parameters of the storage tank as well as physical properties are listed in Table 1. Adaptive time stepping

Table 1  
Geometrical, physical, and operating parameters.

Quantity	Value
Tank dimension, height/diameter	80/50 mm
Initial/inlet temperature, $T_0/T_{in}$	20/20 °C
Inlet pressures, $P$	10.0 bar
Porosity/permeability of the hydride bed, $\epsilon$	$0.3/10^{-8} \text{ m}^2$
Tortuosity of the solid matrix and gas, $\tau^s/\tau^g$	1.5/1.5
Thermal conductivity of the bed, $k^g/k^s$	0.167/2.0 $\text{W m}^{-1} \text{K}^{-1}$
Specific heat capacities, $c_p^g/c_p^s$	14.89/0.419 $\text{kJ kg}^{-1} \text{K}^{-1}$
Activation energy, $E_a$	21179.6 $\text{J mol}^{-1}$
Kinematic viscosity of hydrogen, $\nu^g$	$1.03 \times 10^{-4} \text{ m}^2 \text{s}^{-1}$
Density of the hydride, $\rho^s$	4200 $\text{kg m}^{-3}$
Cooling fluid temperature, $T_\infty$	20 °C
Heat transfer coefficient, $h$	600 $\text{W m}^{-2} \text{K}^{-1}$

is used in which the current time step is inversely proportional to the magnitude of the maximum reaction rate at the previous time step with the maximum of 0.1 s. For iterations in each time step, equation residuals are all smaller than  $10^{-7}$ . A typical simulation takes  $\sim 1$  h.

#### 4. Results and discussion

Fig. 3 compares the model prediction and experimental data. Detail of the experimental setup can be found in Ref. [3]. The reactor tank is cylindrical with geometrical parameters and alloy particle arrangement the same as Scenario #1. The tank was submerged in a bath at a constant temperature ( $T_\infty$ ). In their experiment, three

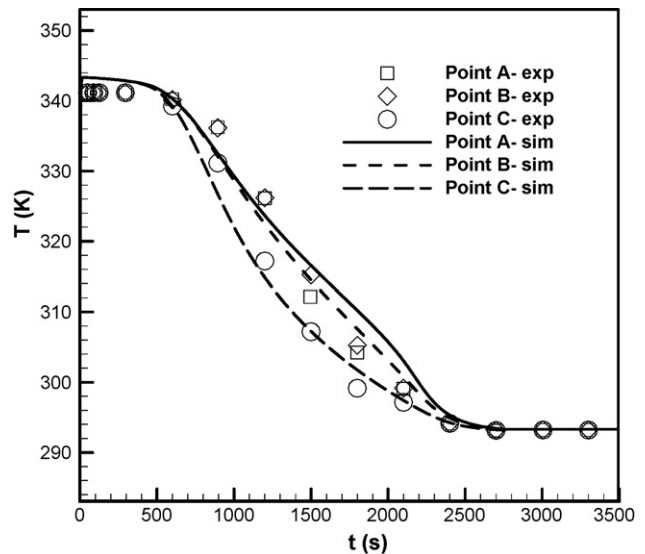


Fig. 3. Validation with experimental data in terms of temperature evolutions (Scenario #1). Experimental data are from Ref. [3]. Point A: located at  $r = 15$  mm and  $z = 35$  mm; Point B: located at  $r = 15$  mm and  $z = 25$  mm; Point C: located at  $r = 15$  mm and  $z = 15$  mm.

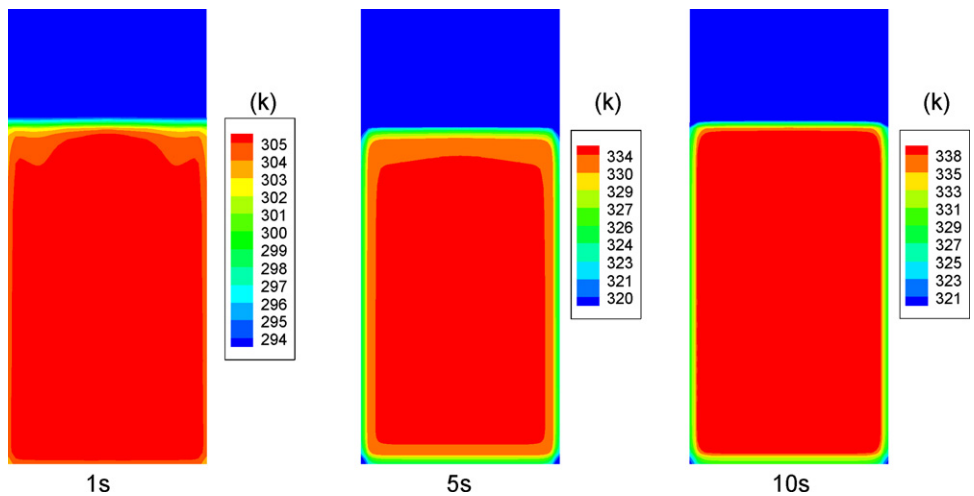


Fig. 4. The temperature distributions in a cross-section of the tank at 1 s, 5 s and 10 s for Scenario #1.

thermal couples were placed within the alloy bed (location A, B, and C) to measure the local temperature evolution. This figure shows a satisfactory agreement. At the beginning, the model over-predicts the temperatures, which may be due to neglecting the heat capacity of the tank wall in the simulation. The validation is based on Scenario #1, where hydrogen is injected from the above.

Figs. 4 and 5 present the evolution of temperature distributions within the tank for Scenario #1. Fig. 4 shows the temperature distributions at the beginning of the fueling (1, 5 and 10 s). It can be seen that the temperature in the porous hydride bed ( $z < 60$  mm) is almost uniform and increases rapidly from the initial temperature. At 1 s, the upper corners near the interface between the alloy bed and expansion space shows different gradient patterns. This is due to the impact of hydrogen flow cooling, which will be explained in detail by the flow fields plotted later. At 5 s, it can be observed that there exist obvious temperature gradients near the wall and upper surface of the metal bed. In particular near the lower corners, the cooling effect cannot be neglected. As the hydride process proceeds, the non-uniformity of the temperature distribution becomes evident in the bed. At 100 s, the area near the wall is much colder than the core region. This is partly due to the slow-down overall reaction rate arising from the depletion of the reactant metal, which reduces

the heat production rate and hence wall temperature. At 2000 s, the high temperature only concentrates in the small region of the core.

Figs. 6 and 7 present the H/M ratio distributions at the six time instants. Fig. 6 shows that the H/M ratio is almost uniform at 1 s, while higher values appear near the wall and the bed upper surface at 5 and 10 s but the spatial variation is fairly small in the hydride bed. Fig. 7 shows the high H/M region increases its area towards the core, where remains a low H/M ratio in most of the time. Even at 2000 s, the hydrogen content in the alloy near the core just reaches about half of the saturation value.

Figs. 8 and 9 display the flow fields at six time instants. It can be seen that the initial velocities are much higher than the ones at the latter stages. At the first second, the velocity is able to reach  $0.2 \text{ m s}^{-1}$ , indicative of a fast reaction rate at the initial stage. The fast kinetics is benefited by the initial lower temperature and H/M ratio. Note that the low H/M ratio also affects the equilibrium pressure,  $P_{eq}$  (see Fig. 1). In the expansion space, the velocity magnitude remains nearly constant, while the velocity in the bed decreases when moving downwards due to the absorption. Similar trends are also shown at other time instants. At the very end stage, i.e. 2000 s, there seems a hydrogen mass sink in the core region, which can be explained by the local higher content of remaining unsaturated

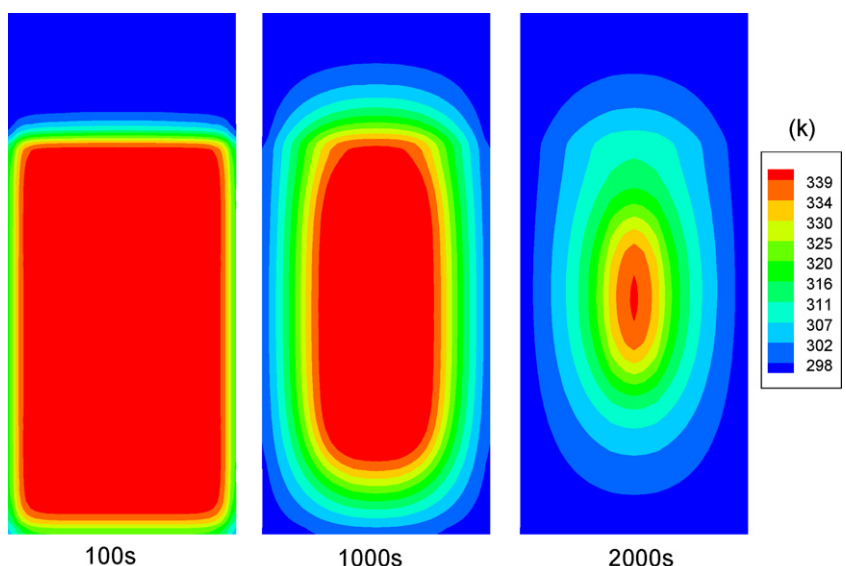


Fig. 5. The temperature distributions in a cross-section of the tank at 100 s, 1000 s and 2000 s for Scenario #1.

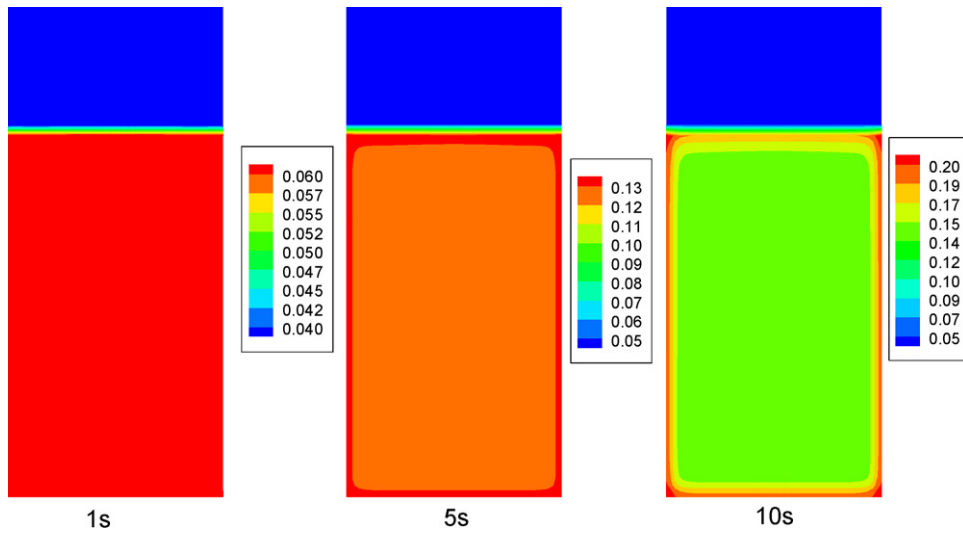


Fig. 6. The H/M ratio or  $(H/M)/(H/M)^s$  distribution in a cross-section of the tank at 1 s, 5 s and 10 s for Scenario #1.

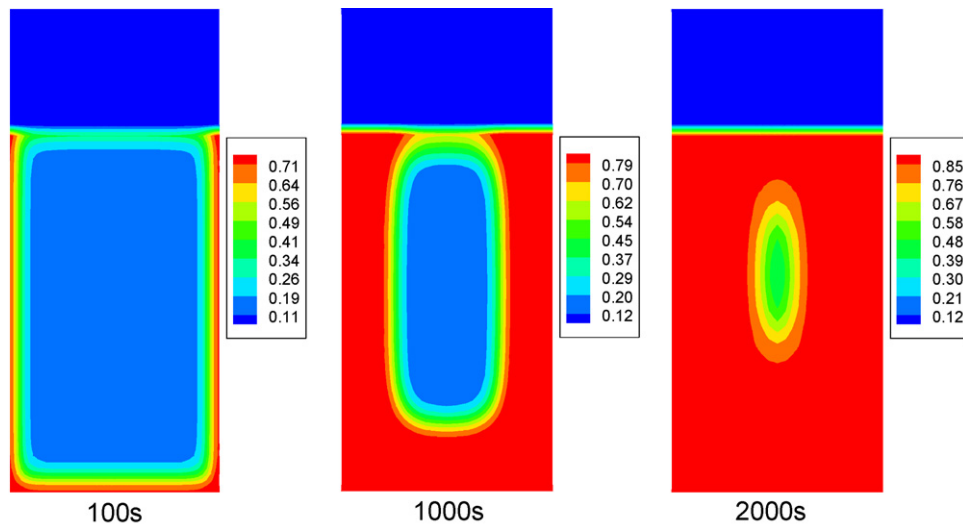


Fig. 7. The H/M ratio or  $(H/M)/(H/M)^s$  distributions in a cross-section of the tank at 100 s, 1000 s and 2000 s for Scenario #1.

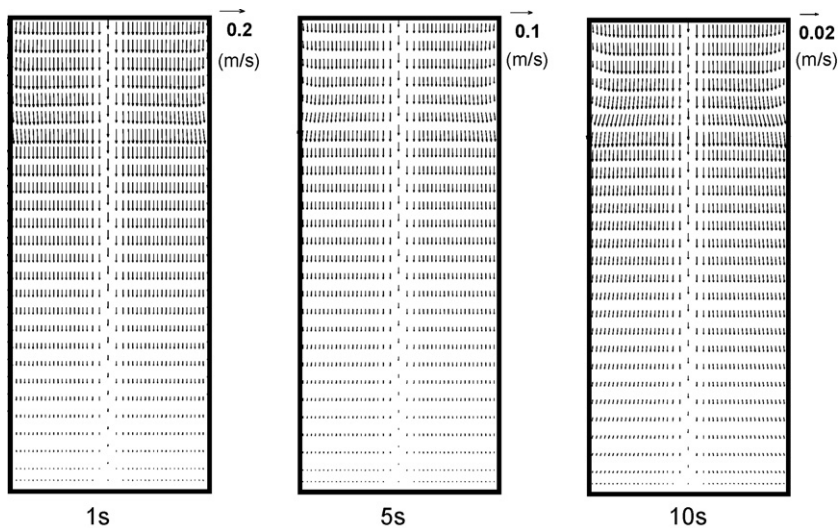


Fig. 8. The velocity distributions in a cross-section of the tank at 1 s, 5 s and 10 s for Scenario #1.

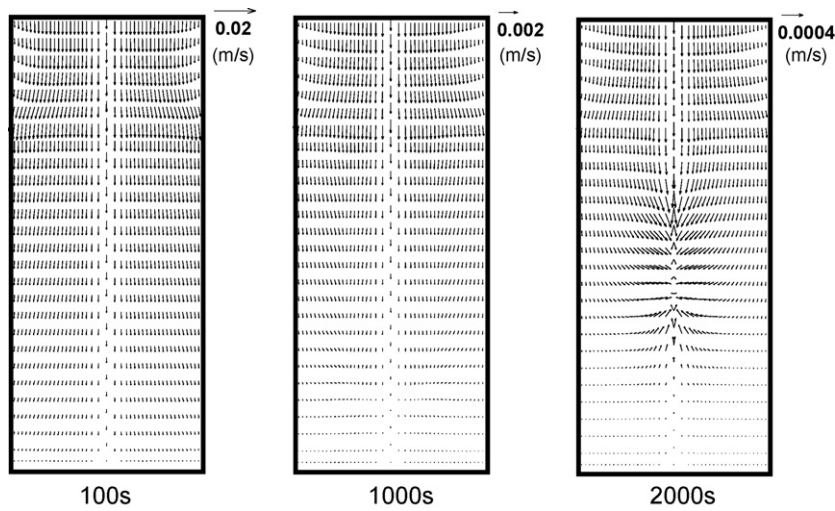


Fig. 9. The velocity distributions in a cross-section of the tank at 100 s, 1000 s and 2000 s for Scenario #1.

metal, as shown in Fig. 7. In addition, except the 1st s, the flow profiles in the expansion region clearly indicate the boundary layer (BL) development near the wall. This is due to the fact that the BL thickness is linear with the reverse of square root of Re (the Reynolds number). At the 1st s, Re is relatively high due to the large flow rate, leading to an almost invisible BL, while in other cases particular at latter stage when the velocity is low, the velocity profile near the wall in the expansion region is evident. In the alloy bed, the Darcy's force dominates and the wall effect becomes negligible. Therefore, when entering the bed, part of the hydrogen mass out of the boundary layer goes towards the wall for the local adsorption, as indicated in these two figures. This lateral flow provides extra cooling. For the strong flow case at the 1st s, the cooling effect is evident, recasting the local temperature distribution at the upper corners of the hydride bed as indicated by the first plot in Fig. 4. Further, a dimensionless number, the Peclet number ( $=Re \times Pr = uR/\alpha$  where  $\alpha$  is the thermal diffusivity), can be used to evaluate the importance of the cooling effect provided by the hydrogen flow. For  $u \sim 0.1 \text{ m s}^{-1}$ ,  $R \sim 25 \text{ mm}$ , and  $\alpha \sim 1.0 \times 10^{-4} \text{ m}^2 \text{ s}^{-1}$ , the Peclet number is  $\sim 25$ , thus convection is dominant. Even with the velocity decreasing to  $\sim 0.01 \text{ m s}^{-1}$  (e.g. at 100 s), convection effect is still comparable

with the conduction (the Peclet number  $\sim 2.5$ ). At 1000 s, the Peclet number is  $\sim 0.5$  in the bed near the inlet, indicating the convection plays an important role in the local heat transfer.

Fig. 10 plots the temperature evolutions of several typical points in the hydride bed. It can be seen that the temperatures near the wall drop fast in the initial stage (Note that there is a jump in temperature at the very beginning when the exothermal reaction heats up the bed as shown in Fig. 4. However, this part is relatively short and not clearly visible in this figure. We exclude our discussion on this period in this paragraph). In particular, the one at the bottom corner decreases fastest. After the initial fast drop, the decreasing pace slows down. In contrast, the two locations in the core region indicate a totally different trend. Initially, their temperatures remain high with little change, followed by sharp drops after  $\sim 1500$  and  $1900 \text{ s}$ , respectively. Fig. 11 shows the evolutions of the mass absorption rates at these locations. It can be seen that the ones near the wall are much faster than the ones near the core in the initial 100 s and decrease nearly exponentially with time. As to the two locations near the core, similar trends are indicated: first decrease partly due to the depletion of the metal, then increase upon the

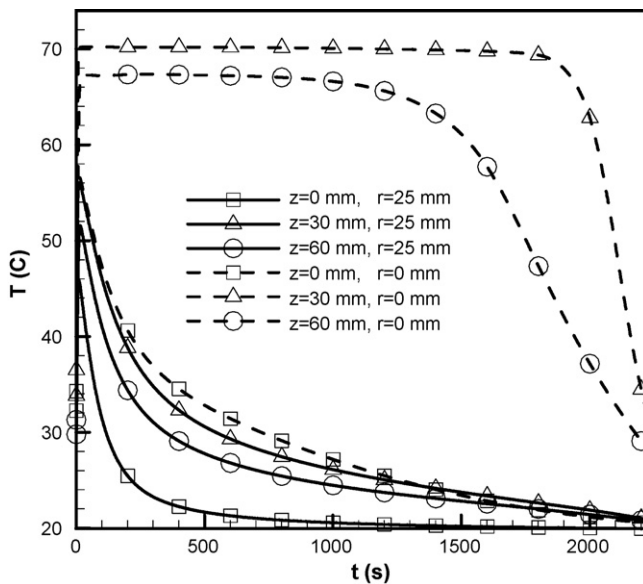


Fig. 10. Evolutions of temperatures at different locations of the tank for Scenario #1.

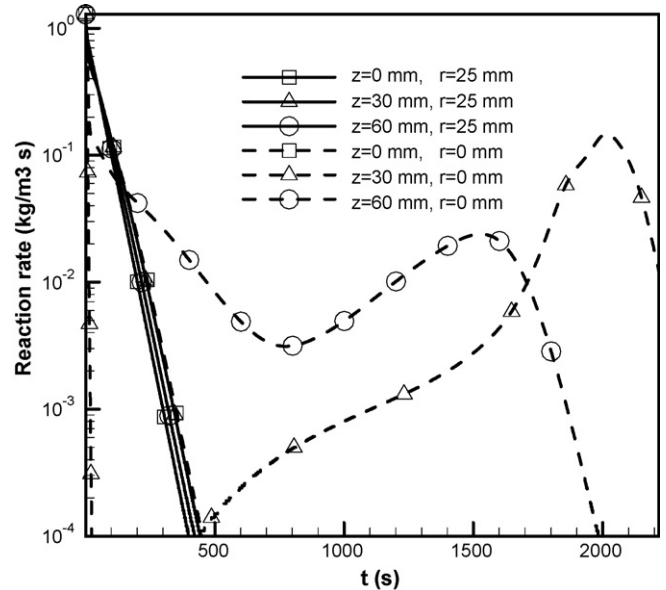


Fig. 11. Evolutions of reaction rates at different locations of the tank for Scenario #1.

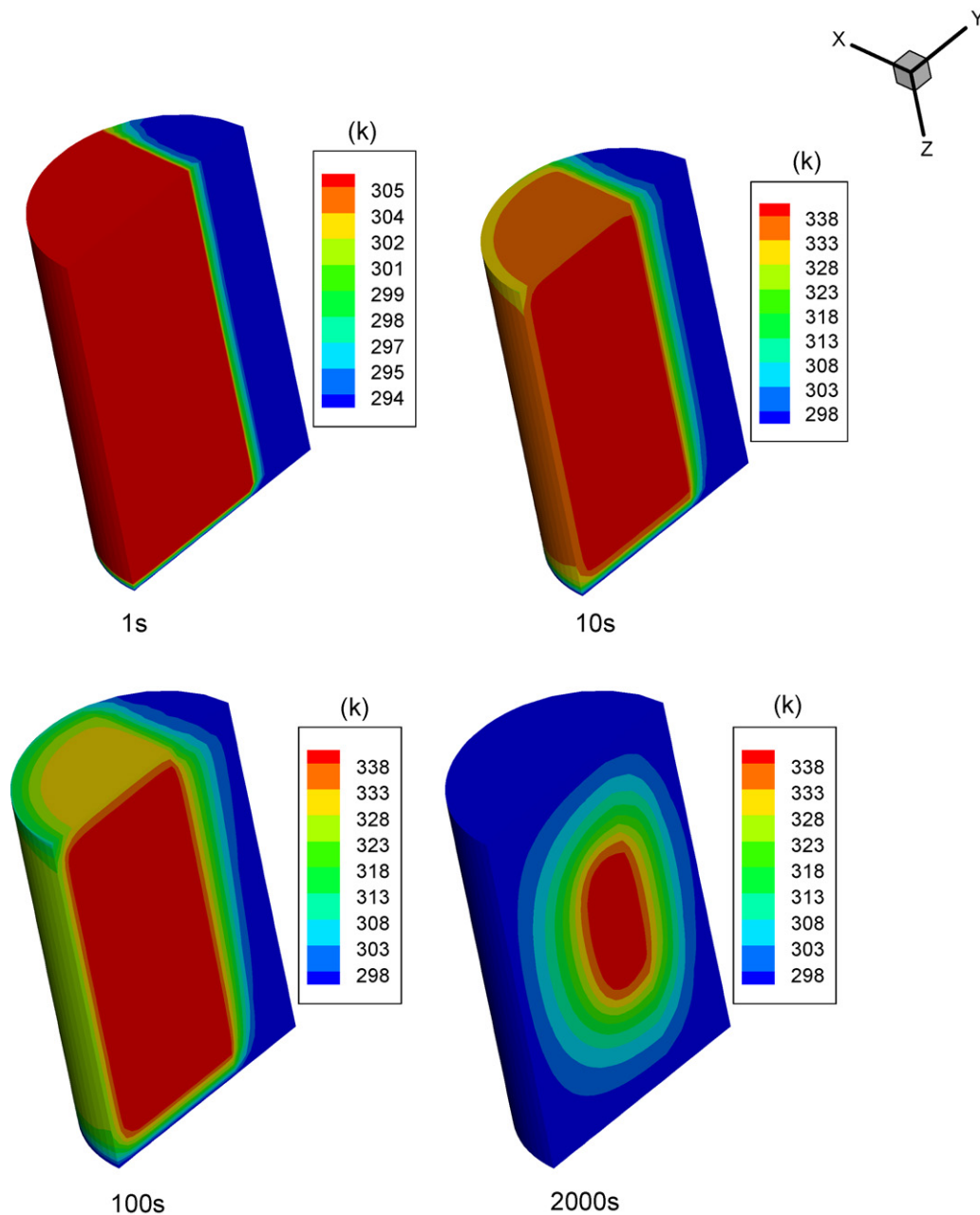


Fig. 12. The temperature distributions in the tank at four time instants for Scenario #2.

temperature drop, followed by another reduction caused by the fact that the metal depletion dominates again. In addition, the middle one, i.e.  $z = 30$  mm and  $r = 0$  mm, falls sharply at the very beginning, several-order-of-magnitude lower than others, which is due to the local high temperature. In addition, even though the reaction at the other point, i.e.  $z = 60$  mm and  $r = 0$  mm, is fast in most time, the temperature is lower as shown in previous figure, which is benefited by the cooling of the hydrogen flow.

As mentioned before, Scenario #1 is essentially a two-dimensional problem, while the problem of Scenario #2 is three-dimensional. Fig. 12 shows the 3D temperature distributions for Scenario #2 at four time instants. Similar to the former case, the bed temperature is almost uniform initially, while varies spatially later with the core at the highest temperature. Fig. 13 shows the velocity distributions. Different with Scenario #1, the velocity in

the expansion is much higher than the one in the hydride bed. In the expansion space, the velocity decreases along the flow due to the bed absorption. In the bed, the flow direction indicates that hydrogen is supplied from both the inlet and expansion region. At 2000 s, hydrogen flow is drawn towards the core where the reaction is still active, similar to Fig. 9. In addition, high velocity in the hydride bed provides extra cooling for the exothermic reaction as shown in Scenario #1. However, repeated hydrogenation/dehydrogenation cycling will cause metal hydride alloy particles pulverized. The hydrogen flow or other external forces such as mechanic shock or vibration may bring the resultant fine particles to the bottom of the cylinder forming a denser layer. This layer will have much lower permeability due to the small pore dimension (see Eq. (3)), affecting the hydrating process. These two effects must be balanced through sophisticate design in practice.

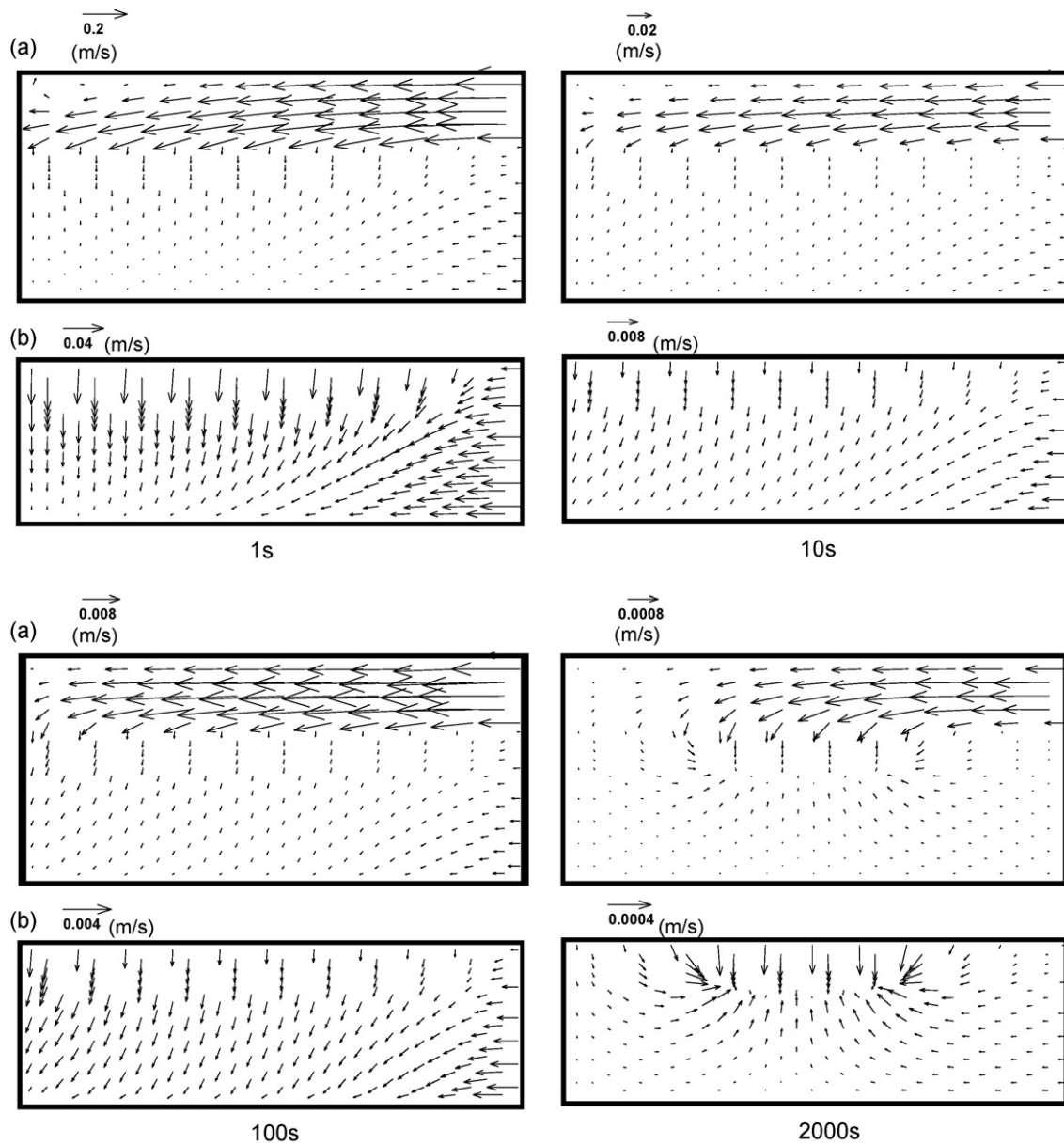


Fig. 13. The velocity distributions in the tank at four time instants for Scenario #2: (a) the middle cross-section of the tank; (b) the middle cross-section of the hydride bed.

**5. Conclusions**

A three-dimensional model was developed to investigate the coupled mass/heat transport phenomena during the absorption process in hydrogen storage tanks. The model consists of principles of mass, momentum, and energy conservations and the absorption kinetics of the metal hydride. Numerical simulations were carried out to reveal the spatial distributions and evolutions of the key quantities within a cylindrical tank for two scenarios. The results indicated that hydrogen absorption is almost uniform at the initial stage but varies spatially at the latter one. In the core region, temperature remains high for quite a long time due to insufficient cooling, followed by a fast drop before the absorption is completed. The initial absorption is fast due to the initial low temperature and H/M ratio. This fast reaction results in a hydrogen flow in the bed with the velocity magnitude much higher than the latter stage. The strong flow also provides extra cooling to the bed near the inlet. Further, we found that the temperature increases rapidly and uniformly at the beginning. It also implies that an optimal thermal

design is important for achieving fast refueling of hydride storage tanks. Future work includes investigating the impacts of parameters on hydrogen fueling, modeling hydrogen desorption process, and integrating the hydrogen tank model with our fuel cell ones [20,21].

**Acknowledgements**

Partial support of this work by the Academic Senate Council on Research, Computing & Library Resources at the UC Irvine is gratefully acknowledged.

**References**

[1] M. Momirlan, T.N. Veziroglu, *Renew. Sustain. Energy Rev.* 6 (2002) 141–179.  
 [2] A. Jemni, S.B. Nasrallah, *Int. J. Hydrogen Energy* 20 (1995) 43–52.  
 [3] A. Jemni, S.B. Nasrallah, J. Lamoumi, *Int. J. Hydrogen Energy* 24 (1999) 631–644.  
 [4] T. Nakagawa, A. Inomata, H. Aoki, T. Miura, *Int. J. Hydrogen Energy* 25 (2000) 339–350.

- [5] M.D. Mat, Y. Kaplan, Int. J. Hydrogen Energy 26 (2001) 957–963.
- [6] M.D. Mat, Y.u. Kaplan, K. Aldas, Int. J. Energy Res. 26 (2002) 973–986.
- [7] B.D. MacDonald, A.M. Rowe, J. Power Sources 161 (2006) 346–355.
- [8] E.S. Kikkinides, M.C. Georgiadis, A.K. Stubos, Energy 31 (2006) 2092–2110.
- [9] A.K. Phate, M.P. Maiya, S.S. Murthy, Int. J. Hydrogen Energy 32 (2007) 1969–1981.
- [10] M.J. MacDonald, C. Chu, P.P. Guilloit, K.M. Ng, AIChE J. 37 (1991) 1583–1588.
- [11] R.C. Bowman Jr., B.D. Craft, A. Attalla, M.H. Mendelsohn, D.M. Gruen, J. Less-Common Met. 73 (1980) 227.
- [12] E.E. Spada, H. Oesterreicher, R.C. Bowman Jr., B.D. Craft, Phys. Rev. B 30 (1984) 4909.
- [13] S.S. Zhang, C.A. Angell, J. Electrochem. Soc. 143 (1996) 4047–4053.
- [14] S. Yagi, D. Kunii, Chem. Eng. Sci. 16 (1961) 634.
- [15] S. Suda, N. Kobayashi, J. Less-Common Met. 73 (1980) 119–126.
- [16] A. Jemni, S.B. Nasrallah, Int. J. Hydrogen Energy 22 (1) (1997) 67–76.
- [17] K. Aldas, M.D. Mat, Y. Kaplan, Int. J. Hydrogen Energy 27 (2002) 1049–1056.
- [18] S.V. Patankar, Numerical Heat Transfer and Fluid Flow, Hemisphere Publishing Corp., New York, 1980.
- [19] H. Dhaou, F. Askri, M. Ben Salah, A. Jemni, S. Ben Nasrallah, J. Lamloumi, Int. J. Hydrogen Energy 32 (2007) 576–587.
- [20] Y. Wang, C.Y. Wang, Electrochim. Acta 50 (2005) 1307–1315.
- [21] Y. Wang, J. Power Sources 185 (2008) 261–271.